Engineering built-in electric fields through p-n heterojunction construction for enhanced dual-functional water electrolysis in Co_2P/Fe_2P systems

Ang Li, Baiyu Ren, Heng Yang, Hui Min Gu, Bao Yue Zhang, Nikhil V. Medhekar, Xinyi Hu, Hao Yu, Yinfen Cheng, Yuefeng Yin, Zhong Li, Jian Zhen Ou

PII: S0925-8388(26)02474-6

DOI: https://doi.org/10.1016/j.jallcom.2026.188405

Reference: JALCOM188405

To appear in: *Journal of Alloys and Compounds*

Received date: 9 March 2026
Revised date: 30 April 2026
Accepted date: 30 April 2026

Please cite this article as: Ang Li, Baiyu Ren, Heng Yang, Hui Min Gu, Bao Yue Zhang, Nikhil V. Medhekar, Xinyi Hu, Hao Yu, Yinfen Cheng, Yuefeng Yin, Zhong Li and Jian Zhen Ou, Engineering built-in electric fields through p-n heterojunction construction for enhanced dual-functional water electrolysis in Co_2P/Fe_2P systems, *Journal of Alloys and Compounds,* (2026) doi:https://doi.org/10.1016/j.jallcom.2026.188405

Engineering built-in electric fields through p-n heterojunction construction for enhanced dual-functional water electrolysis in Co_2P/Fe_2P systems

Ang Li [a 1], Baiyu Ren [b 1], Heng Yang [a], Hui Min Gu [a], Bao Yue Zhang [d***], Nikhil V. Medhekar [c], Xinyi Hu [a], Hao Yu [e], Yinfen Cheng [f], Yuefeng Yin [c**], Zhong Li [a*], Jian Zhen Ou [a,d*]

[a] Key Laboratory of Advanced Technologies of Materials, Ministry of Education, School of Materials Science and Engineering, Southwest Jiaotong University, Chengdu 610031, China

[b] School of Materials Engineering, Mianyang Polytechnic, Mianyang, China

[c] Department of Materials Science and Engineering, Monash University, Australia

[d] School of Engineering, RMIT University, Melbourne, Victoria 3000, Australia

[***] Corresponding authors at: School of Engineering, RMIT University, Melbourne, Victoria 3000, Australia.

E-mail addresses: Baoyue.zhang@rmit.edu.au.

[**] Corresponding authors at: Department of Materials Science and Engineering, Monash University, Australia.

E-mail addresses: yuefeng.yin@monash.edu.

[*] Corresponding authors at: Key Laboratory of Advanced Technologies of Materials, Ministry of Education, School of Materials Science and Engineering, Southwest Jiaotong University, Chengdu 610031, PR China.

E-mail addresses: zhong.li@swjtu.edu.cn.

[*] Corresponding authors at: Key Laboratory of Advanced Technologies of Materials, Ministry of Education, School of Materials Science and Engineering, Southwest Jiaotong University, Chengdu 610031, PR China.

E-mail addresses: jianzhen.ou@rmit.edu.au, jzou@swjtu.edu.cn(J.Z. Ou).

1 These authors contribute equally to this work.

[e] Xihua University, Jinzhou Road, Chengdu, Sichuan 610039, China

[f] Institute for Advanced Study, Chengdu University, Chengdu 610106, China

ARTICLE INFO

Keywords：

Water Splitting

p-n Heterojunctions

Dual-functional Catalysts

Hydrogen Evolution Reaction (HER)

Oxygen Evolution Reaction (OER)

Built-in Electric Field

ABSTRACT

The rational design of heterostructured electrocatalysts with efficient charge transfer pathways is crucial for advancing sustainable water-splitting technology. In this work, a bimetallic Co_2P/Fe_2P heterojunction catalyst is successfully synthesized on nickel foam (NF) through a hydrothermal method followed by controlled phosphorization. The heterointerface between Co_2P and Fe_2P induces a strong built-in electric field (BEF) due to their distinct Fermi level alignment, as confirmed by Mott-Schottky analysis and Kelvin probe force microscopy (KPFM). This BEF gives rise to electron-deficient Co regions and electron-enriched Fe regions near the heterointerface, which is expected to modulate the local electronic structure and facilitate interfacial charge transfer, thereby benefiting the overall HER/OER kinetics. The as-prepared

Co_2P/Fe_2P@NF exhibits exceptional bifunctional activity in alkaline media, achieving low overpotentials of 109 mV for the hydrogen evolution reaction (HER) and 165 mV for the oxygen evolution reaction (OER) at 20 mA cm^{-2}, with Tafel slopes of 54.8 mV dec^{-1} and 31.5 mV dec^{-1}, respectively. A two-electrode electrolyzer assembled with Co_2P/Fe_2P@NF as both anode and cathode requires only 1.50 V to deliver 20 mA cm^{-2}, surpassing most reported non-noble metal catalysts. Systematic characterizations (XPS, TEM, EIS) reveal that the hierarchical nanoplate structure with abundant heterointerfaces provides a high electrochemical surface area (17.4 mF cm^{-2}) and facilitates electrolyte penetration. Moreover, the catalyst exhibits outstanding long-term durability, retaining at least 98% of its initial performance after 20 h of continuous operation at 20 mA cm^{-2} under both oxygen evolution reaction (OER) and hydrogen evolution reaction (HER) conditions. This work highlights the pivotal role of interfacial BEF engineering in developing high-performance electrocatalysts for practical water-splitting applications.

1. Introduction

Facing the worsening global energy crisis and environmental problems caused by the overuse of fossil fuels, developing green and efficient hydrogen production technology through water electrolysis has become a key solution to achieving carbon neutrality goals [1]. The water-splitting process faces limitations due to the four-electron transfer mechanism in the anodic oxygen evolution reaction (OER) and the

high energy barrier in the cathodic hydrogen evolution reaction (HER), leading to low overall efficiency [2, 3]. Currently, noble metal-based catalysts (e.g., Pt/C, IrO_2) show excellent performance, but their high cost and scarcity severely hinder large-scale applications [4]. Therefore, developing low-cost transition metal-based bifunctional catalysts with high activity has become a research hotspot [5, 6]. Recent reviews on non-precious transition-metal-based HER catalysts further emphasize that transition-metal phosphides, heterostructure construction, defect modulation, morphology engineering, and electronic-structure tailoring are key strategies for developing durable and cost-effective water-electrolysis catalysts [7, 8].

Transition metal phosphides (TMPs), especially Co_2P and Fe_2P, exhibit promising HER/OER bifunctionality in alkaline media owing to their good electrical conductivity and tunable semiconducting electronic structures [9]. However, single-component TMPs still face several inherent challenges. Single-phase catalysts often struggle to balance the adsorption/activation requirements of HER intermediates (H*) and OER intermediates (OH*, O*, and OOH*) [10, 11]. In addition, bulk materials usually suffer from limited electrochemically accessible surface area, while conventional synthesis routes tend to induce agglomeration of active sites [12, 13]. More importantly, under harsh anodic OER conditions, TMPs tend to undergo surface oxidation/reconstruction into metal oxyhydroxide-related active layers; although such self-reconstruction can generate catalytically active species, it may also cause structural instability, metal leaching, and electron-transport losses [14-17]. Therefore, recent TMP catalyst design

has increasingly shifted from merely improving apparent activity toward regulating the parent phosphide framework, reconstructed surface species, and interfacial electronic structure simultaneously[9, 16].

Recent CoFeP phosphide heterostructures further demonstrate that crystalline/amorphous interfacial engineering can induce work-function-driven charge redistribution and generate built-in electric fields, thereby modulating the electronic structure and improving bifunctional HER/OER kinetics under alkaline water-electrolysis conditions [18]. In particular, constructing heterojunctions with a built-in electric field (BEF) has emerged as an effective strategy to promote directional electron transfer, generate electron-rich/electron-deficient interfacial regions, and lower kinetic barriers during electrocatalysis [19-21]. For example, a recent NiCoP/FeP p-n heterojunction study demonstrated that the work-function-driven BEF can induce electron accumulation/depletion zones at the phosphide interface, optimize the d-band center and hydrogen adsorption free energy, and thereby improve alkaline HER activity and stability [19]. Similarly, a Ni_2P/CoP_2 heterojunction nanoarray was reported to accelerate charge redistribution through a BEF directed from Ni_2P to CoP_2, leading to enhanced alkaline overall water-splitting performance [20]. Beyond activity enhancement, recent studies have also highlighted that BEF engineering can guide OER surface reconstruction by promoting electron transfer and asymmetric charge distribution, thereby improving catalytic activity and stability [22]. Recent CoP-containing heterostructures further confirm that BEF-driven directional electron

transfer can create electron-deficient and electron-rich interfacial regions that regulate the adsorption of key reaction intermediates [23]. Therefore, it is highly desirable to select appropriate building blocks to construct TMP-based bifunctional catalysts and to explore in depth how the BEF strength correlates with interfacial charge transfer and catalytic behavior in both HER and OER. While Co_2P/Fe_2P composites have shown promise, prior studies have mainly focused on apparent activity enhancement [24, 25]. A quantitative understanding of the interfacial BEF and its relationship with charge-transfer behavior and intrinsic catalytic activity remains elusive. This knowledge gap limits the rational design of p-n heterojunctions in which the direction and magnitude of the BEF are pivotal for regulating interfacial electronic structure and improving water-splitting kinetics.

Herein, we deliberately design and fabricate the bimetallic heterostructure of Co_2P/Fe_2P nanoplates arrays grown on nickel foam (NF) for alkaline overall water splitting. Using CoFe-LDH as a precursor, the phosphorization process retains a 3D porous nanoplate structure (Fig. 1a-b), ensuring abundant active sites and fast electrolyte penetration. Combining KPFM with Mott-Schottky analysis, we estimated an effective interfacial built-in electric field of ~9.26×10^6 V m^{-1} across the n-Co_2P/p-Fe_2P junction (ΔV = 0.25 V and Δx = 27 nm; Fig. 3a-f), which supports directional charge transfer from Co_2P to Fe_2P and efficient charge separation [26]. The resulting asymmetric interfacial electron redistribution is expected to modulate the local electronic environments of Co and Fe sites, thereby facilitating interfacial charge

transfer and promoting dual-functional electrocatalytic kinetics [27]. Electrochemically, Co_2P/Fe_2P@NF exhibits excellent bifunctional activity in 1 M KOH (HER: η_{20} = 109 mV; OER: η_{20} = 165 mV) together with good stability (>20 h @ 20 mA cm^{-2}). Moreover, a homemade electrolyzer assembled with Co_2P/Fe_2P@NF as both the cathode and anode requires only 1.50 V to achieve 20 mA cm^{-2}, outperforming most previously reported non-noble-metal-based electrocatalysts [28, 29].

2. Experimental section

2.1. Reagents and materials

All materials and chemical reagents were purchased from Chengdu Cologne Chemical Co., Ltd., or Aladdin and used without further purification. The chemicals included cobalt nitrate hexahydrate, ammonium fluoride, ferric nitrate nonahydrate, sodium hypophosphite monohydrate, and urea.

2.2. Pretreatment of NF

Before the subsequent experiments, several pieces of nickel foam (NF, 1 × 2 cm, surface density: 350 mg cm^{-2}, thickness: 1.0 mm) were sequentially ultrasonically cleaned in dilute hydrochloric acid, acetone, and anhydrous ethanol for 30 minutes each, then rinsed thoroughly with deionized water, and dried under vacuum at 60°C for 6 hours.

2.3. Preparation of Co_2P/Fe_2P

CoFe-LDH nanoarrays were grown on nickel foam (NF) through a hydrothermal

synthesis protocol. Specifically, 0.5 mmol cobalt nitrate hexahydrate $Co(NO_3)_2 \cdot 6H_2O$, 0.5 mmol ferric nitrate $Fe(NO_3)_3 \cdot 9H_2O$, 10 mmol urea, and 4 mmol ammonium fluoride (NH_4F) were dissolved in 30 mL deionized water under vigorous stirring to form a homogeneous precursor solution. A clean piece of nickel foam was then immersed in the reaction solution, transferred to a 50 mL autoclave, and heated at 120°C for 6 hours. After cooling to room temperature, the resulting CoFe-LDH/NF was washed thoroughly with deionized water and dried in a vacuum oven at 60°C for 12 hours. Using the same method, $Co(OH)_2$/NF and $Fe(OH)_2$/NF were also obtained.

For phosphorization, 200 mg of sodium hypophosphite monohydrate ($NaH_2PO_2 \cdot H_2O$) was placed in a porcelain boat at the upstream side of the tube furnace, while the precursor CoFe-LDH/NF was placed in another porcelain boat at the downstream side. The furnace was then heated to 350 °C at a ramping rate of 5 °C min^{-1} and maintained for 2 h under flowing Ar (50 sccm).

The catalyst loading amount on the nickel foam was approximately 1.7 mg cm^{-2}. All electrodes used for electrochemical comparison were prepared on nickel foam substrates with the same geometric area (1 × 2 cm^2) under identical synthesis conditions.

2.4. Physical characterization

The obtained samples were characterized using various techniques to analyze their morphologies and properties. Optical microscopy (OM, SDPTOP CX40M), scanning electron microscopy (SEM, FEI Inspect F50), and atomic force microscopy (AFM,

Korea Park NX10) were employed for morphological assessment. To study the microstructure of the synthesized samples, transmission electron microscopy (TEM, JEM-F200) was carried out, with an acceleration voltage of 200 kV. The constituent elements of the samples were confirmed through X-ray powder diffraction (XRD, PANalytical diffractometer, Cu-Kα radiation) and X-ray photoelectron spectroscopy (XPS, Thermo Scientific K-Alpha). Ultraviolet-visible (UV-Vis) spectroscopy was performed using a Shimadzu UV-2600 spectrophotometer to examine the optical properties. Scanning transmission electron microscopy (STEM, JEOL ARM200F) was used for detailed imaging, while Kelvin probe force microscopy (KPFM) enabled the measurement of the sample's work function and surface potential.

2.5. Electrochemical measurements

All electrochemical tests were conducted at room temperature using a three-electrode system on a CHI 660E electrochemical workstation, with 1.0 M KOH as the electrolyte (purged with nitrogen for 15 minutes to remove dissolved oxygen). The Hg/HgO electrode served as the reference electrode, while a graphite rod was employed as the counter electrode.

Linear sweep voltammetry (LSV) was carried out at a scan rate of 5 mV s^{-1}. In this study, each LSV curve was corrected with 90% iR compensation according to the equation: $E_{corr} = E_{mea} - iR_s$. Here, E_{corr} denotes the corrected potential, E_{mea} the directly measured potential, and R_s the ohmic resistance of the solution as determined by EIS. All potentials were converted to the reversible hydrogen electrode (RHE) scale

according to the following equation: $E_{RHE}= E_{Hg/HgO} + 0.098 + 0.059$ pH, where the pH of 1 M KOH is 14. Electrochemical impedance spectroscopy (EIS) was employed to assess the charge-transfer resistance at the interface between the electrode and electrolyte. The measurements were carried out at applied potentials of 0.6 V and -1.2 V (vs. RHE) over a frequency range from 10^5 Hz to 0.01 Hz, with an AC voltage amplitude set to 5 mV. Cyclic voltammetry (CV) measurements were conducted at scan rates from 20 to 120 mV s^{-1} within the non-faradaic potential regions of 0.2-0.3 V and 1.05-1.15 V (vs. RHE) to determine the double-layer capacitance (C_{dl}), and the electrochemically active surface area (ECSA) was calculated by dividing C_{dl} by the specific capacitance (Cs). The ECSA-normalized current density (j_{ECSA}) was calculated according to $j_{ECSA}=j_{geo}\times C_s/C_{dl,}$ where j_{geo} is the geometric current density, C_s is the specific capacitance of bare NF. Because the specific capacitance of bare NF depends on the non-faradaic potential window, the C_s values used for normalization were determined separately in the HER and OER regions, giving 0.98 mF cm^{-2} for HER and 3.64 mF cm^{-2} for OER, and C_{dl} is the double-layer capacitance of the catalyst. The calculated ECSA values are summarized in Table S3, and the corresponding ECSA-normalized HER and OER polarization curves are shown in Fig. S15. To evaluate the catalyst's intrinsic activity, the Tafel slope was derived using the equation: $\eta = a + x \log |j|$, where "η" represents the overpotential, "|j|" is the absolute current density, "a" is the Tafel constant, and "x" is the Tafel slope. Long-term HER and OER stability tests were conducted by chronopotentiometry at a constant current density of 20 mA cm^{-2} for 20

h in 1.0 M KOH. No stirring, gas purging, or electrolyte replacement was applied during the measurements. Tafel slopes were obtained by linear fitting of the well-defined kinetically controlled regions (i.e., the low-overpotential linear regions) of the polarization curves. For the Co_2P/Fe_2P catalyst, the representative fitting ranges were approximately 100-160 mV for HER and 150-195 mV for OER.

To ensure the reliability of the electrochemical data, HER and OER polarization measurements were repeated at least three times using independently prepared electrodes. The catalytic performance was highly reproducible with negligible variations (Fig. S14), and the representative curves are presented in the manuscript.

2.6. Density functional theory (DFT) calculations

Spin-polarized density functional theory (DFT) calculations were carried out using the Vienna ab initio simulation package (VASP) with the projector augmented wave (PAW) method and the generalized gradient approximation in the Perdew-Burke-Ernzerhof (GGA-PBE) form. A plane-wave cutoff energy of 500 eV was adopted. All structures were relaxed until the total-energy change was below 1×10^{-5} eV and the residual forces were less than 0.02 eV Å. Monkhorst-Pack *k*-point meshes of 7×7×7 for bulk models and 5×5×1 for slab/interface models were employed. A coherent Co_2P (112)/Fe_2P (111) interface with a lattice mismatch below 3% was constructed. A vacuum layer thicker than 15 Å was introduced along the surface normal, the bottom atomic layers were fixed during relaxation, and a dipole correction was applied along the normal slab. For density-of-states (DOS) calculations, a denser *k*-mesh (up to

9×9×1) together with a Gaussian smearing of 0.05 eV was used. The charge-density difference (CDD) was defined as $\Delta\rho = \rho_{hetero} - \rho_{Co_2P} - \rho_{Fe_2P}$, where $\rho_{Co_2P}$and ρ_{Fe_2P} were calculated in the same supercell and grid as the heterostructure with atomic positions fixed. Isosurfaces of $\pm 2 \times 10^{-3}$ e $Å^{-3}$ were used for visualization. The Fermi level (E_F) was set to 0 eV as energy reference.

3. Results and discussion

3.1. Phase and microstructure

The synthetic route of the Co_2P/Fe_2P heterostructure can be briefly divided into two steps, as schematically illustrated in Scheme 1. First, CoFe-LDH nanoplate arrays were grown on an NF substrate (denoted as CoFe-LDH/NF) via a facile hydrothermal method [30]. Subsequently, CoFe-LDH/NF was used as a precursor and converted to bimetallic phosphides through a low-temperature phosphorization process, resulting in the fabrication of the Co_2P/Fe_2P heterostructure on NF (denoted as Co_2P/Fe_2P@NF).

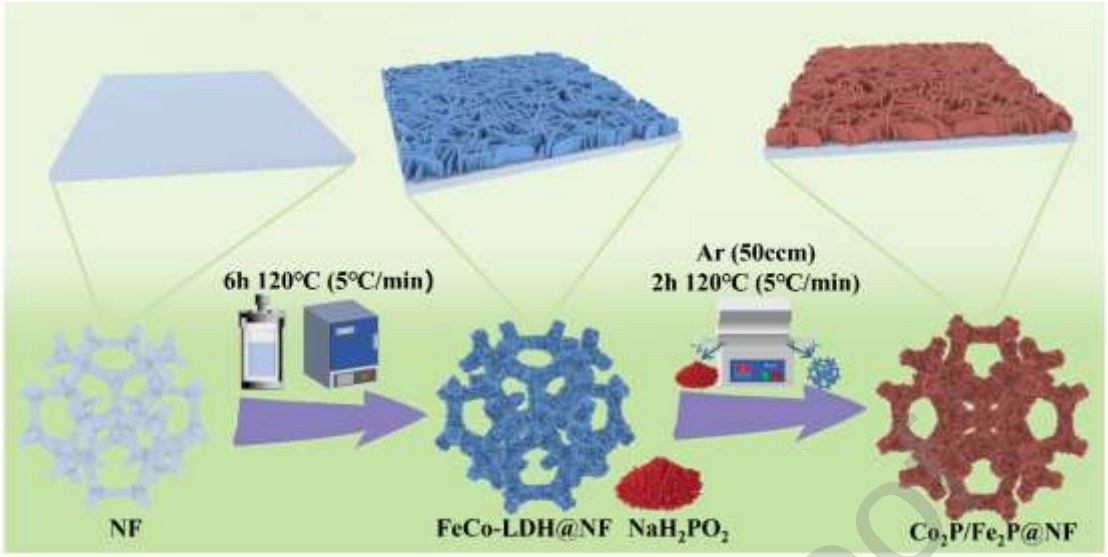

Scheme 1. Schematic illustration for the synthetic process of Co_2P/Fe_2P nanoplates.

Field-emission scanning electron microscopy (FE-SEM) images of Co_2P/Fe_2P @NF are shown in Fig. 1a-b. After phosphorization, the resulting Co_2P/Fe_2P exhibits large-scale lamellar-structured nanoplates with a thickness of approximately 60 to 100 nm and a length of about 0.5 to 1.5 μm, interconnected with each other. These nanoplates are oriented either slantwise or perpendicular to the NF substrate, creating numerous apparent porous structures. The macroporous Co_2P/Fe_2P 3D nanoarray skeleton derived from CoFe-LDH retains its structural integrity (Fig. S1). However, the thickness significantly increases, with no reduction in the number or size of the pores. Consequently, this augments the specific surface area and enhances the exposure of catalytically active sites. A high specific surface area and large porosity can provide abundant active regions between the electrode and electrolyte, which is beneficial for electron transport [31]. This usually proves highly beneficial in augmenting catalytic performance.

SEM-EDS elemental mapping (Fig. 1c) reveals the homogeneous distribution of Co, Fe, and P throughout the Co_2P/Fe_2P nanoplates, confirming the successful formation of the heterostructure. SEM-EDS analysis further indicates slight surface oxidation, while phosphorization remains successful (Fig. S2 and Table S1).

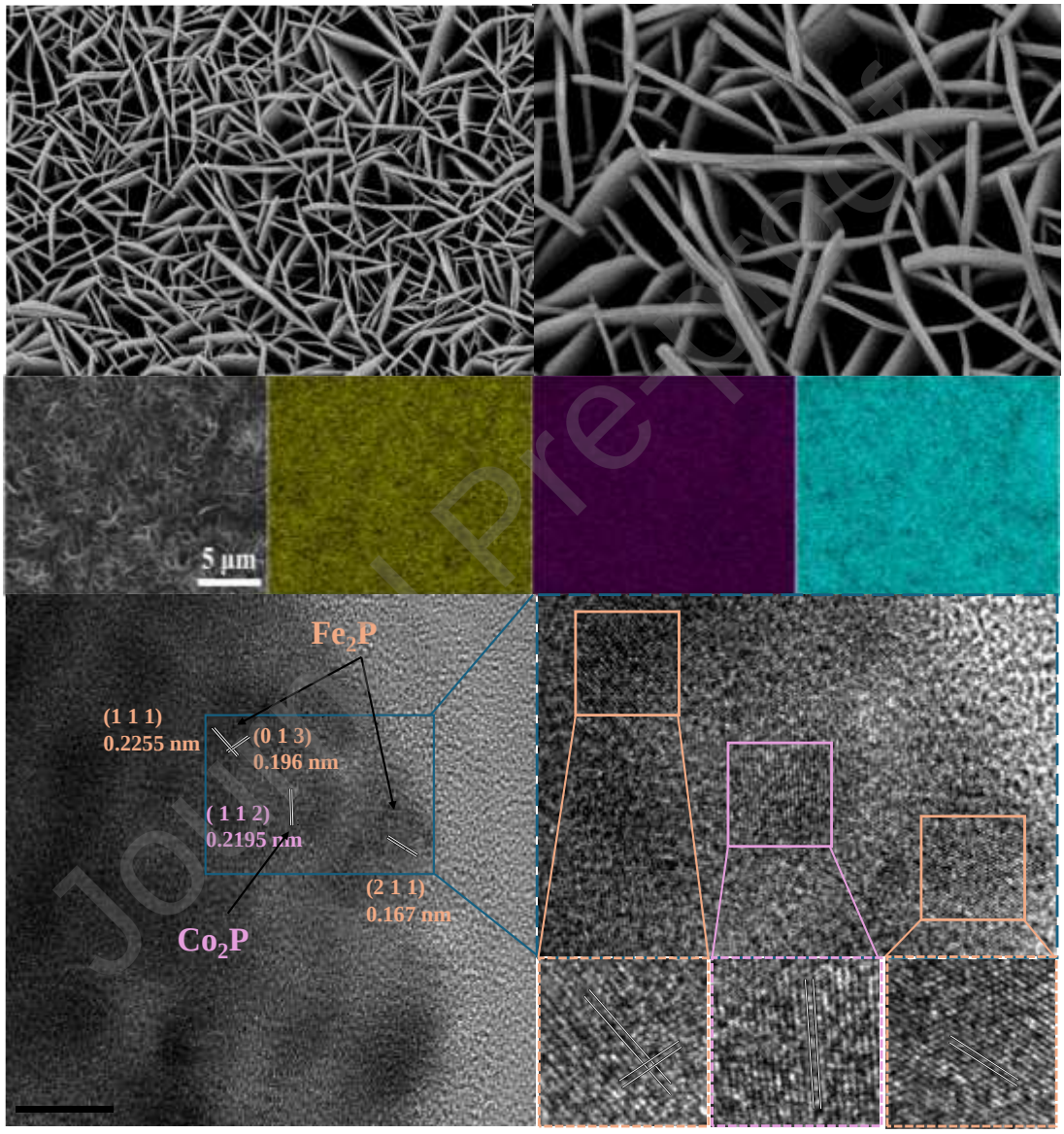

Fig. 1. SEM images of (a, b) Co_2P/Fe_2P nanoplate; (c) SEM-EDS mapping of Co_2P/Fe_2P; (d) TEM and HRTEM images of Co_2P/Fe_2P.

To further examine the detailed nanostructure of Co_2P/Fe_2P nanoplates, TEM and

HRTEM analyses were conducted. As shown in Fig. 1d, the Co_2P/Fe_2P nanoplates can be readily exfoliated into thinner nanosheets, exhibiting extensive cracking and numerous holes uniformly distributed throughout the nanoplates. After phosphating, the original morphology is preserved, facilitating electrolyte penetration into active sites and the removal of gas bubbles during the water-splitting process. The as-obtained Co_2P/Fe_2P nanoplates become rougher and thicker with porous nanostructures, which is expected to increase the catalyst surface area and improve mass transport capability. HRTEM images reveal that the crystalline nanoparticles of Co_2P and Fe_2P, tightly embedded into the nanoplates, are in close contact with each other, producing heterogeneous interfaces. The well-resolved lattice fringes with spacing distances of 0.2195 nm correspond well to the (1 1 2) planes of Co_2P. Similarly, the high-resolution lattice fringes with d-spacings of 0.2255 nm, 0.1960 nm, and 0.1670 nm correspond well to the (1 1 1), (0 1 3), and (2 1 1) planes of Fe_2P, respectively, further confirming the heterointerface structure between Co_2P and Fe_2P. These results are also verified by the Fast Fourier Transformation (FFT) pattern in the Fig. S4.

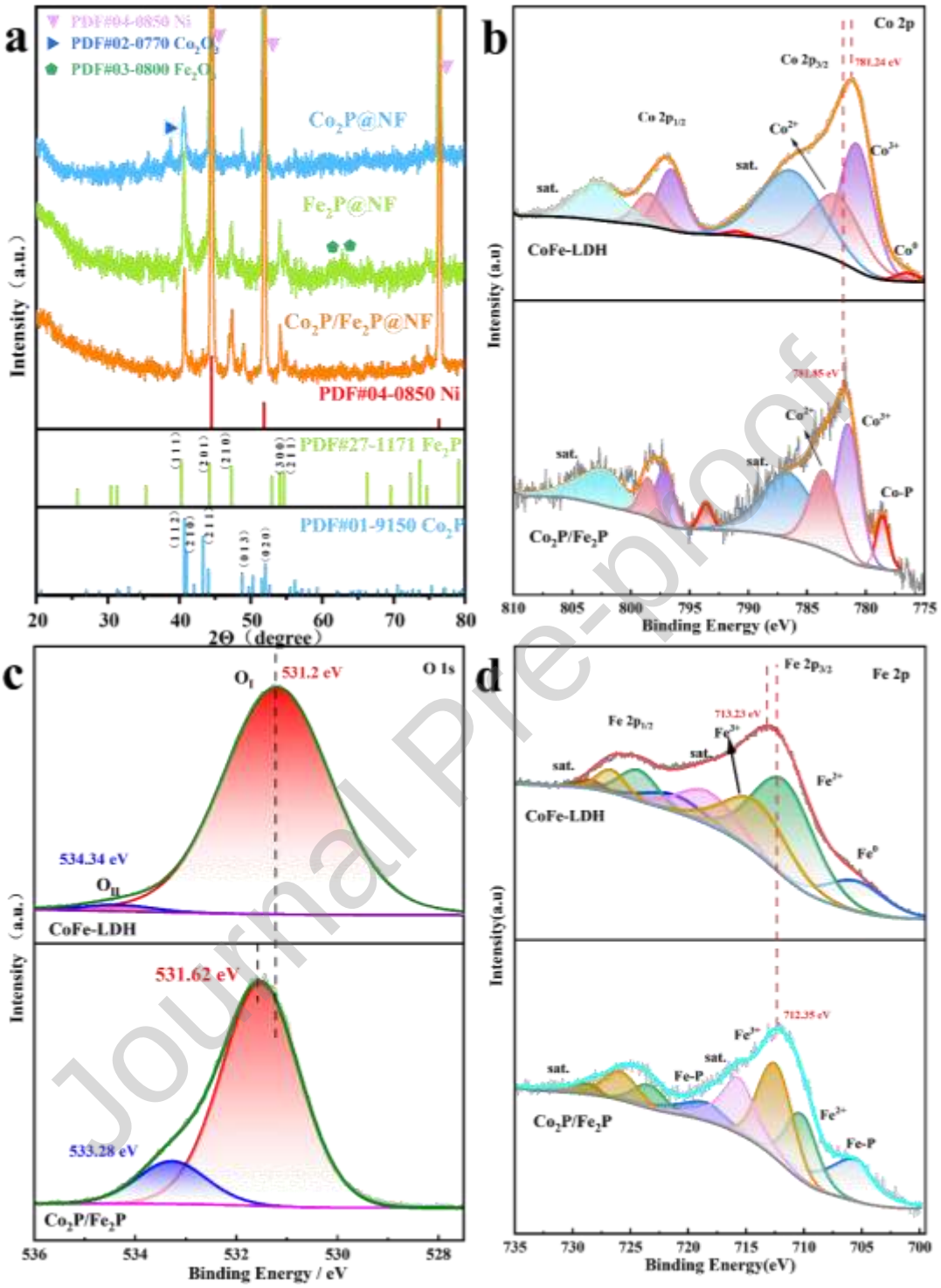

Fig. 2. (a) XRD patterns of Co_2P/Fe_2P, Co_2P, and Fe_2P. XPS spectra: (b) Co 2p, (c) O 1s, and (d) Fe 2p of Co_2P/Fe_2P and FeCo-LDH. X-ray diffraction (XRD) was then used to further analyze the crystal structure of the material (Fig. 2a). Fe_2P, Co_2P, and

Co_2P/Fe_2P are used as comparisons, and both perfectly match their respective standard cards. The X-ray diffraction (XRD) pattern of Co_2P/Fe_2P@NF shows characteristic peaks at 2θ values of 40.72°, 40.98°, 43.3°, 48.76°, and 52.07°, which can be indexed to the (1 1 2), (2 1 0), (2 1 1), (0 1 3), and (0 2 0) crystal planes of orthorhombic Co_2P (PDF#04-001-9150). Meanwhile, other characteristic peaks at 40.28°, 42.19°, 47.31°, 54.10°, and 54.62° match well with the (1 1 1), (2 0 1), (2 1 0), (3 0 0) and (2 1 1) planes of tetragonal Fe_2P (PDF#00-027-1171). Additionally, a slight oxidation is observed for both Co_2P and Fe_2P. In the XRD pattern of Co_2P, the peak at 38.61° corresponds to the (1 0 2) crystal plane of Co_2O_3. Similarly, the peaks of Fe_2P at 62.26° and 63.69° are assigned to the (2 1 4) and (3 0 0) crystal planes of Fe_2O_3, respectively. Three strong peaks at 2θ values of 44.5°, 51.8°, and 76.4° are assigned to the Ni foam substrate (PDF#00-04-0850). X-ray photoelectron spectroscopy (XPS) was employed to investigate the elemental composition and surface chemical states of CoFe-LDH and Co_2P/Fe_2P nanoplates. The XPS survey spectrum in Fig. S3a confirmed the presence of Co, Fe, O and P elements in the Co_2P/Fe_2P heterojunctions, in good agreement with the elemental mapping results shown in Fig. 1c. The high-resolution P 2p XPS spectrum of Co_2P/Fe_2P in Fig. S3b displayed three characteristic peaks at 129.50, 130.33, and 133.85 eV, which were attributed to P $2p_{3/2}$, P $2p_{1/2}$, and oxidized P species, respectively. In the high-resolution Co 2p XPS spectrum (Fig. 2b), Co_2P/Fe_2P exhibited peaks corresponding to Co^{3+} at 781.47 eV and 797.11 eV, and Co^{2+} at 783.56 eV and 798.55 eV. These peaks were accompanied by two satellite peaks at 786.56 eV and 802.10 eV.

The peaks at 778.56 eV and 793.60 eV were attributed to Co-P bonds. Notably, the Co 2p peaks in Co_2P/Fe_2P showed a positive shift compared to the original CoFe-LDH, suggesting a reduction in the charge density around the Co atoms after the formation of the heterostructure. Regarding the Fe element (Fig. 2d), Co_2P/Fe_2P exhibited Fe^{3+} peaks at 712.49 eV and 725.89 eV, and Fe^{2+} peaks at 710.12 eV and 723.35 eV. The presence of both Fe^{3+} and Fe^{2+} species suggests their origin from surface-oxidized Fe-PO_x species. These peaks were also accompanied by two satellite peaks at 715.67 eV and 728.48 eV. The peaks at 705.48 eV and 718.28 eV were attributed to Fe-P bonds. Compared to CoFe-LDH, the Fe 2p peaks in Co_2P/Fe_2P exhibited a negative shift in binding energy, indicating an increase in the charge density around the Fe atoms after the formation of the heterostructure [32]. These results further confirm the electron transfer from Co_2P to Fe_2P and the successful establishment of a built-in electric field (BEF) in the Co_2P/Fe_2P heterojunction, which leads to electron-deficient Co regions and electron-enriched Fe regions near the interface. These results support the formation of an interfacial BEF from Co_2P to Fe_2P, which is expected to facilitate charge separation and interfacial charge transfer. The resulting local electronic modulation is further consistent with improved HER/OER kinetics [32]. Beyond these favorable structural features, the intrinsic interfacial electronic coupling within the Co_2P/Fe_2P heterojunction was further investigated to understand its underlying catalytic mechanism.

3.2. Electronic structure and built-in electric field analysis

To reveal the origin and magnitude of the interfacial built-in electric field (BEF) in the Co_2P/Fe_2P heterostructure, we analyzed the semiconductor type, band alignment, and local surface potential distribution.

Semiconductor type and band alignment. As shown by the Mott-Schottky (M-S) responses (Fig. 3d, e), Co_2P and Fe_2P behave as oppositely doped semiconductors, which enables the construction of a p-n junction. This assignment is consistent with our overall electronic-structure analysis, where Co_2P exhibits n-type characteristics and Fe_2P shows p-type characteristics. Accordingly, the band alignment derived from the M-S results together with the optical bandgap information (Fig. 3f) indicates a favorable junction configuration that drives spontaneous interfacial charge redistribution upon contact [33].

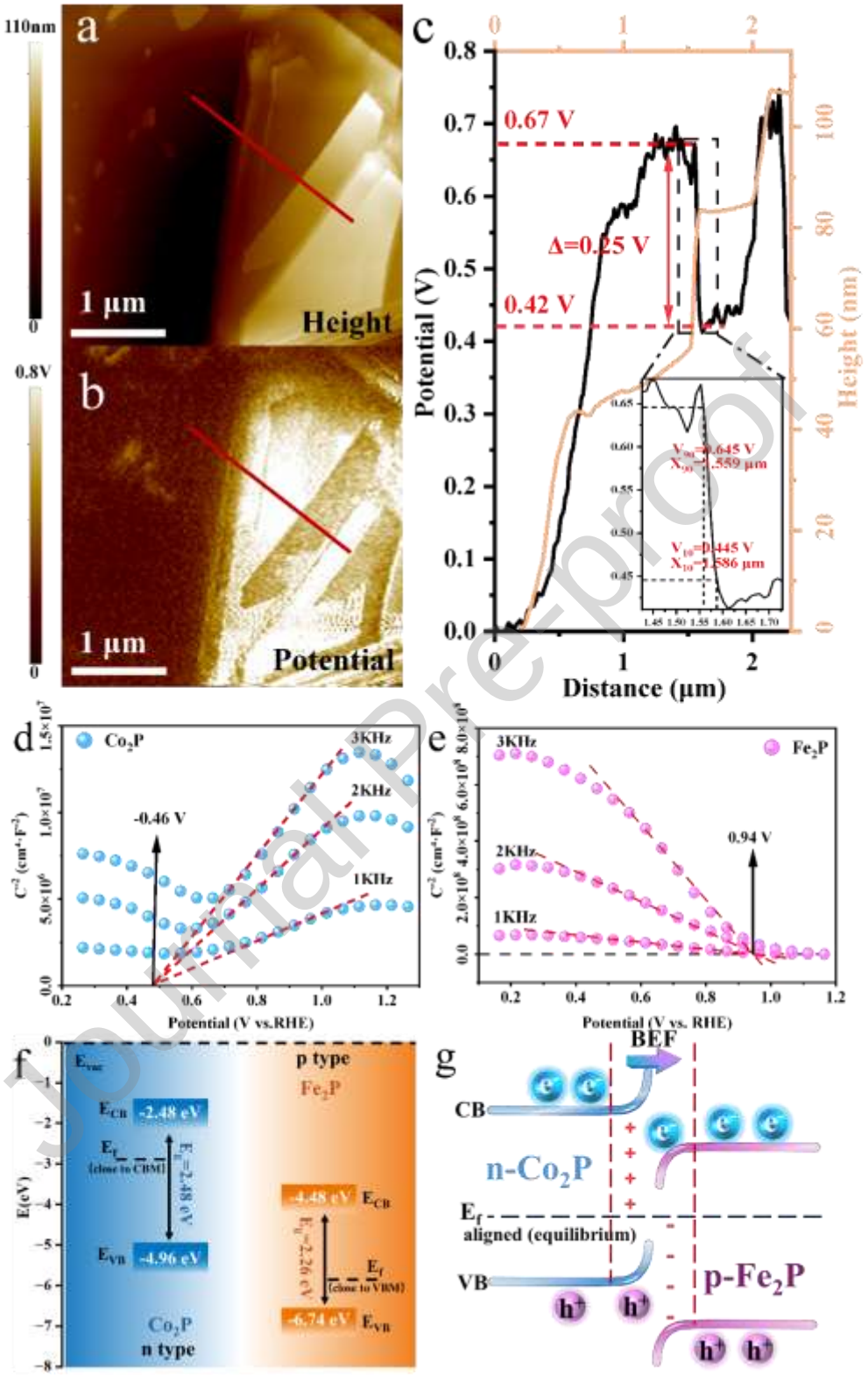

Fig. 3. (a) AFM topography and (b) KPFM surface potential maps of Co_2P/Fe_2P. (c) Corresponding height and potential profiles across the interface. Mott-Schottky plots of (d) Co_2P and (e) Fe_2P. (f) Band alignments of the pristine phases. (g) Schematic of the charge transfer and built-in electric field in the Co_2P/Fe_2P p-n heterojunction.

Experimental evidence of interfacial charge redistribution. XPS corroborates the interfacial electron transfer after heterojunction formation: the Co 2p peaks show a positive shift while the Fe 2p peaks shift negatively, confirming electron migration from Co_2P to Fe_2P and the generation of electron-deficient Co sites and electron-enriched Fe sites. This interfacial charge redistribution is the thermodynamic origin of the BEF and underpins the electronic modulation at the heterointerface.

KPFM visualization and quantitative BEF estimation. Scanning Kelvin probe force microscopy (SKPFM) was further employed to directly probe the local contact potential difference across the heterointerface. The SKPFM height and surface-potential maps (Fig. 3a, b) and the corresponding line profile (Fig. 3c) show a clear potential step across the Co_2P/Fe_2P boundary, with two plateau potentials of 0.67 V and 0.42 V, yielding an interfacial potential drop of ΔV = 0.25 V. To avoid subjective estimation of the transition width, we adopted the standard 10%-90% step-width method using the values marked in Fig. 3c (V_{90} = 0.645 V at x_{90} = 1.559 μm; V_{10} = 0.445 V at x_{10} = 1.586 μm), giving $\Delta x = x_{10} - x_{90}$ = 0.027 μm = 27 nm. Therefore, the effective interfacial built-in electric field is estimated as $E_{avg}=\Delta V/\Delta x \approx 9.26 \times 10^6$ V m^{-1} [30, 34, 35]. It should be noted that Δx represents an apparent transition width that can be affected by electrostatic averaging and tip convolution in KPFM; nevertheless, the pronounced ΔV and the derived E_{avg} provide quantitative evidence for a strong solid-solid interfacial driving force that facilitates directional charge migration across the junction.

Furthermore, since electrocatalysis proceeds in liquid electrolyte, the interfacial charging behavior was evaluated by zeta-potential measurements (Fig. S8). The Co_2P/Fe_2P heterojunction exhibits a higher zeta potential (35.2 mV) than Co_2P (25.5 mV) and Fe_2P (9.58 mV), indicating enhanced interfacial charge density and a strengthened electric double layer (EDL), which is beneficial for ion accumulation and interfacial reaction kinetics at the catalyst-electrolyte interface [26].

3.3. Electrochemical performances and mechanism analysis of HER and OER

Given the electronic modulation by the strong BEF in Co_2P/Fe_2P heterojunctions, the intrinsic electrocatalytic activity of Co_2P/Fe_2P is expected to be largely influenced [36].

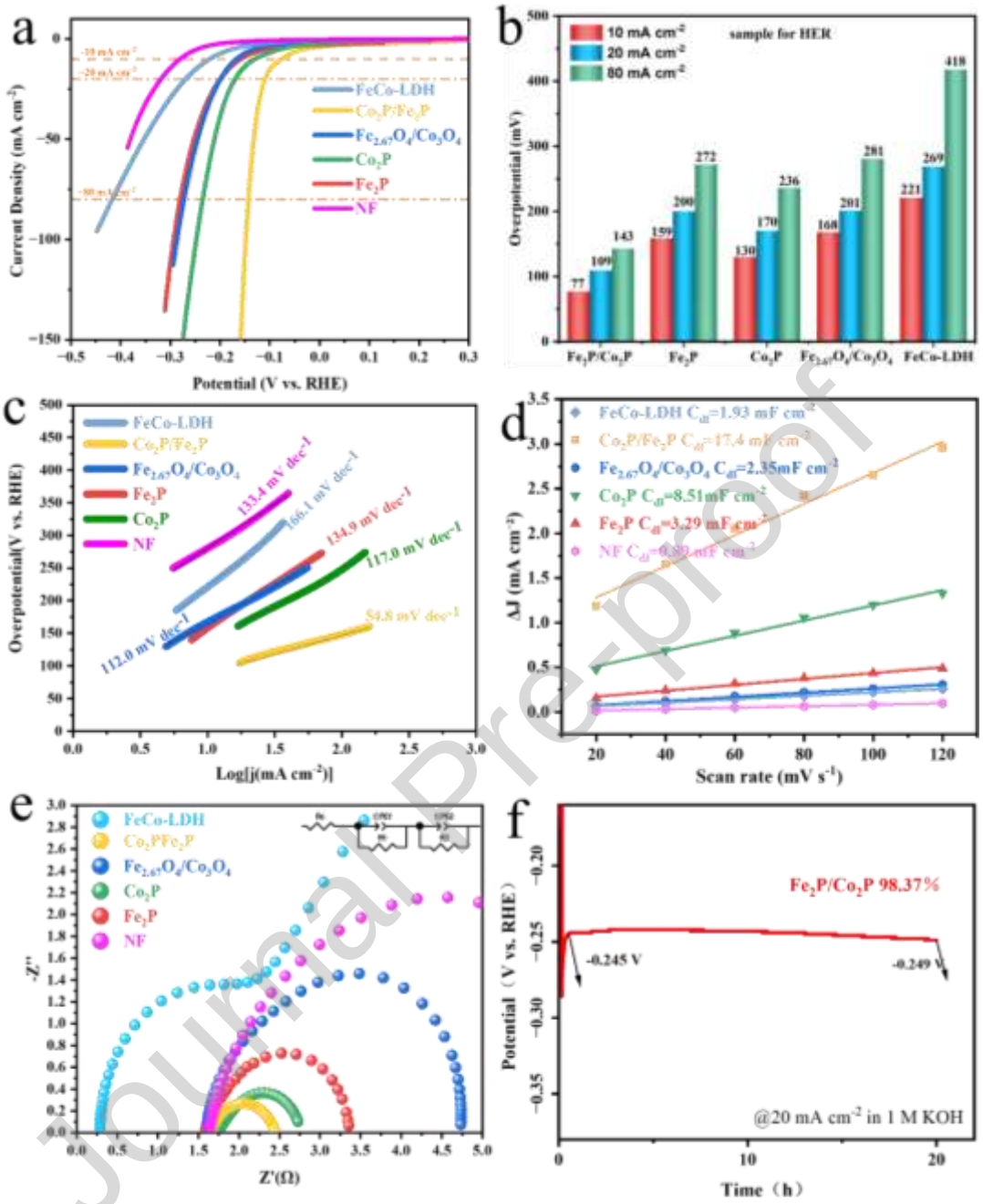

Fig. 4. HER of Co_2P/Fe_2P, Fe_2P, Co_2P, CoFe-LDH, $Fe_{2.67}O_4/Co_3O_4$ and pure NF. (a) LSV curves at a scan rate of 5 mV s^{-1}; (b) the overpotentials at 10, 20, and 80 mA cm^{-2}; (c) Tafel plots; (d) double-layer capacitance measurements (plot of scan rate vs. current density) for HER of Co_2P/Fe_2P, Fe_2P, Co_2P, CoFe-LDH, $Fe_{2.67}O_4/Co_3O_4$ and pure NF; (e) Nyquist plots of Co_2P/Fe_2P, Fe_2P, Co_2P, $Fe_{2.67}O_4/Co_3O_4$, FeCo-LDH, and NF; (f) Chronopotentiometry curve of Co_2P/Fe_2P at 20 mA cm^{-2} for 20 h in 1.0 M KOH.

HER measurements were first performed in a typical three-electrode system in 1 M KOH. As compared, pure NF, pristine CoFe-LDH, Co_2P, Fe_2P, and CoFe oxides were

also measured under the same conditions. As shown in the IR-corrected linear sweep voltammetry (LSV) curves in Fig. 4a, Co_2P/Fe_2P reveals a low overpotential of 79 mV at a current density of 10 mA cm^{-2}, significantly lower than that of pure NF, pristine CoFe-LDH, Co_2P, and CoFe oxides. Importantly, this excellent HER activity is highly reproducible across independently prepared electrodes (Fig. S14a). Meanwhile, corresponding Tafel plots in Fig. 4c indicate a small value of 54.8 mV dec^{-1} for Co_2P/Fe_2P via fitting the linear region from the Tafel equation ($\eta=b \log j+a$, where η refers to overpotential, b for Tafel slope, j for current density, and a for Tafel constant), superior to the other counterparts, confirming the distinctly preferred HER kinetics of Co_2P/Fe_2P [37, 38]. The electrochemically active surface areas (ECSA) were further explored to evaluate their intrinsic activities. The double-layer capacitances (C_{dl}) extracted by plotting the capacitive current densities of non-Faradaic regions as a function of scan rates (Fig. S9) are utilized to obtain ECSA. As shown in Fig. 4d, the calculated double-layer capacitance (C_{dl}) value of 17.4 mF cm^{-2} for Co_2P/Fe_2P is significantly higher than that of CoFe-LDH/NF, which is 1.93 mF cm^{-2}. This indicates a substantial increase in the active surface area of LDHs before and after the phosphating process, attributed to the formation of phosphides during the phosphorization process [39]. Notably, the ECSA increases by 17-fold for the Co_2P/Fe_2P/NF compared to the CoFe-LDH/NF. However, from the pristine LDHs to $Fe_{2.67}O_4/Co_3O_4$, there is no significant difference in ECSA, but the overpotential shows a notable variation. This comparison demonstrates conclusively that ECSA alone

cannot account for the enhanced catalytic performance, which aligns with the significantly reduced Tafel slope discussed earlier. To further decouple the contribution of active surface area from intrinsic catalytic activity, the ECSA-normalized HER polarization curves were calculated (Fig. S15a) based on the ECSA values summarized in Table S3. Even after normalization by ECSA, Co_2P/Fe_2P still exhibits the highest HER activity among all samples at the same overpotential, indicating that the superior HER performance cannot be attributed solely to the enlarged active surface area [40]. Instead, the result supports intrinsically enhanced HER kinetics induced by the heterointerface and BEF-driven electronic modulation. It is worth mentioning that the phosphating process not only increases the number of active sites but also significantly enlarges the overall electrochemically accessible surface area [39, 41]. Electrochemical impedance spectroscopy (EIS) measurements were performed to study the charge-transfer capability at the electrode/electrolyte interface. As shown in Fig. 4e and Table S2, Co_2P/Fe_2P shows the smallest charge-transfer resistance (R_{ct}), demonstrating that Co_2P/Fe_2P favors the electrocatalytic kinetics of HER by improving the charge transfer rate [42].

Table 1 Comparison of OER and HER performances of phosphides.

Catalysts	Electrolyte	Overpotential (mV) (oer)	Overpotential (mV) (her)	Tafel slope (mVdec-1)	Refs.
CoP_2 FeP_4/IF	1 M KOH	253 (10 mA cm^{-2})	115 (10 mA cm^{-2})	35.8 / 87.4	[43]
FeP-CoP	1 M KOH	230 (10 mA cm^{-2})	-	90.3 / -	[10]
FeP/CoP	1 M KOH	247 (10 mA cm^{-2})	-	68.1 / -	[44]
NiCoP	1 M KOH	101 (10 mA cm^{-2})	250 (10 mA cm^{-2})	57.5 / 72.3	[34]
PtP_2/CoP	1 M KOH	298 (100 mA cm^{-2})	115 (100 mA cm^{-2})	44.7 / 72.0	[45]

$MnNiCo_2P$	1 M KOH	245 (10 mA cm^{-2})	129 (10 mA cm^{-2})	- / -	[46]
Co_2P/Ni_2P/CNT	1 M KOH	-	202 (10 mA cm^{-2})	- / 58.0	[47]
Co-Fe_2P	1 M KOH	274 (100 mA cm^{-2})	138 (100 mA cm^{-2})	45.0 / 57.0	[32]
FeCoP/$Ni(OH)_2$	1 M KOH	206 (10 mA cm^{-2})	91 (10 mA cm^{-2})	32.0 / 48.0	[48]
NiCoP	1 M KOH	238 (10 mA cm^{-2})	43 (10 mA cm^{-2})	96.0 / 64.1	[49]
Co_2P/Fe_2P	1 M KOH	157 (10 mA cm^{-2})	77 (10 mA cm^{-2})	31.5 / 54.8	**This**

The OER measurement of Co_2P/Fe_2P was also conducted in a three-electrode system. As shown in Fig. 5a, the LSV curves exhibit superior OER activity for the heterostructure Co_2P/Fe_2P compared to pure NF, pristine CoFe-LDH, Co_2P, Fe_2P, and CoFe oxide. The heterostructure Co_2P/Fe_2P achieves the lowest overpotential of 157 mV at a current density of 10 mA cm^{-2} (Fig. 5b), significantly lower than most reported transition metal phosphides (Table 1) [10, 12, 50]. Moreover, the heterostructure Co_2P/Fe_2P demonstrates more rapid reaction kinetics with a low Tafel slope of 31.5 mV dec^{-1}, as shown in Fig. 5c. Additionally, Co_2P/Fe_2P exhibits the largest C_{dl} value of 31.7 mF cm^{-2} and the smallest R_{ct} of 0.509 Ω, as determined by EIS and ECSA measurements, respectively, as shown in Fig. 5d (Table S2) and Fig. 5e. This indicates enhanced charge transfer dynamics and a higher density of active sites on the surface. Similarly, the ECSA-normalized OER polarization curves (Fig. S15b) further confirm the intrinsic catalytic advantage of Co_2P/Fe_2P. After eliminating the surface-area contribution using the ECSA values listed in Table S3, Co_2P/Fe_2P still outperforms the single-phase phosphides and oxide/LDH controls at the same normalized current density. This result indicates that the outstanding OER activity arises not merely from a larger electrochemically accessible surface area, but also from intrinsically enhanced kinetics associated with the heterointerface [51, 52]. The long-term stability test reveals

excellent stability for the heterostructure Co_2P/Fe_2P, with negligible degradation of current density over an extended period (Fig. 5f) [28, 37]. An increase in the anodic peak around 1.4 V, associated with the oxidation of Co(II)/Fe(II), is observed after phosphating (Fig. S11), suggesting that the phosphating process makes more active sites accessible [13, 53, 54]. After conducting long-term stability tests under high current densities during OER and HER, XRD pattern analysis was performed comparing Co_2P/Fe_2P and $Fe_{2.67}O_4/Co_3O_4$ before and after the tests. The study revealed that the characteristic peaks indicative of phosphorization did not significantly diminish or disappear after prolonged operation, and no new peaks indicative of oxidation appeared [55]. This further corroborates the material's excellent long-term stability (as shown in Fig. S12).

To further probe the surface evolution of the Co_2P/Fe_2P catalyst after OER, post-OER XPS measurements were carried out (Fig. S16). The survey spectrum (Fig. S16 a) confirms that Co, Fe, O, and P remain present on the catalyst surface after OER, while the strong O signal indicates the formation of an oxygen-rich reconstructed surface. In the high-resolution O 1s spectrum (Fig. S16 b), two major components centered at 530.30 and 531.26 eV can be assigned to metal-oxygen (M-O) species and hydroxyl/oxyhydroxide- and phosphate-related oxygen species, respectively, indicating a hydroxylated/oxidized surface environment. The post-OER Co 2p spectrum (Fig. S16 c) is dominated by oxidized Co species with mixed Co^{2+}/Co^{3+} characteristics, accompanied by broad shake-up satellite features, whereas the characteristic Co-P

signal is strongly weakened or nearly absent. Similarly, the Fe 2p spectrum (Fig. S16 d) is mainly governed by oxidized Fe species with Fe^{2+}/Fe^{3+} characteristics and broad high-binding-energy multiplet/satellite-related features, while only a weak residual Fe-P component can still be resolved, suggesting that the original phosphide environment is largely suppressed after OER. In the P 2p region (Fig. S16 e), the low-binding-energy phosphide-P component is strongly weakened, whereas oxidized phosphorus species in the ~133 eV region become dominant, indicating substantial phosphorus oxidation and the formation of a phosphate/POx-rich reconstructed surface layer. Taken together, these post-OER XPS results demonstrate that the Co_2P/Fe_2P precatalyst undergoes pronounced in-situ surface oxidation/reconstruction during OER, leading to an oxidized/oxyhydroxide- and phosphate-rich surface layer, while the bulk phosphide framework is still largely retained according to the post-test XRD results [56].

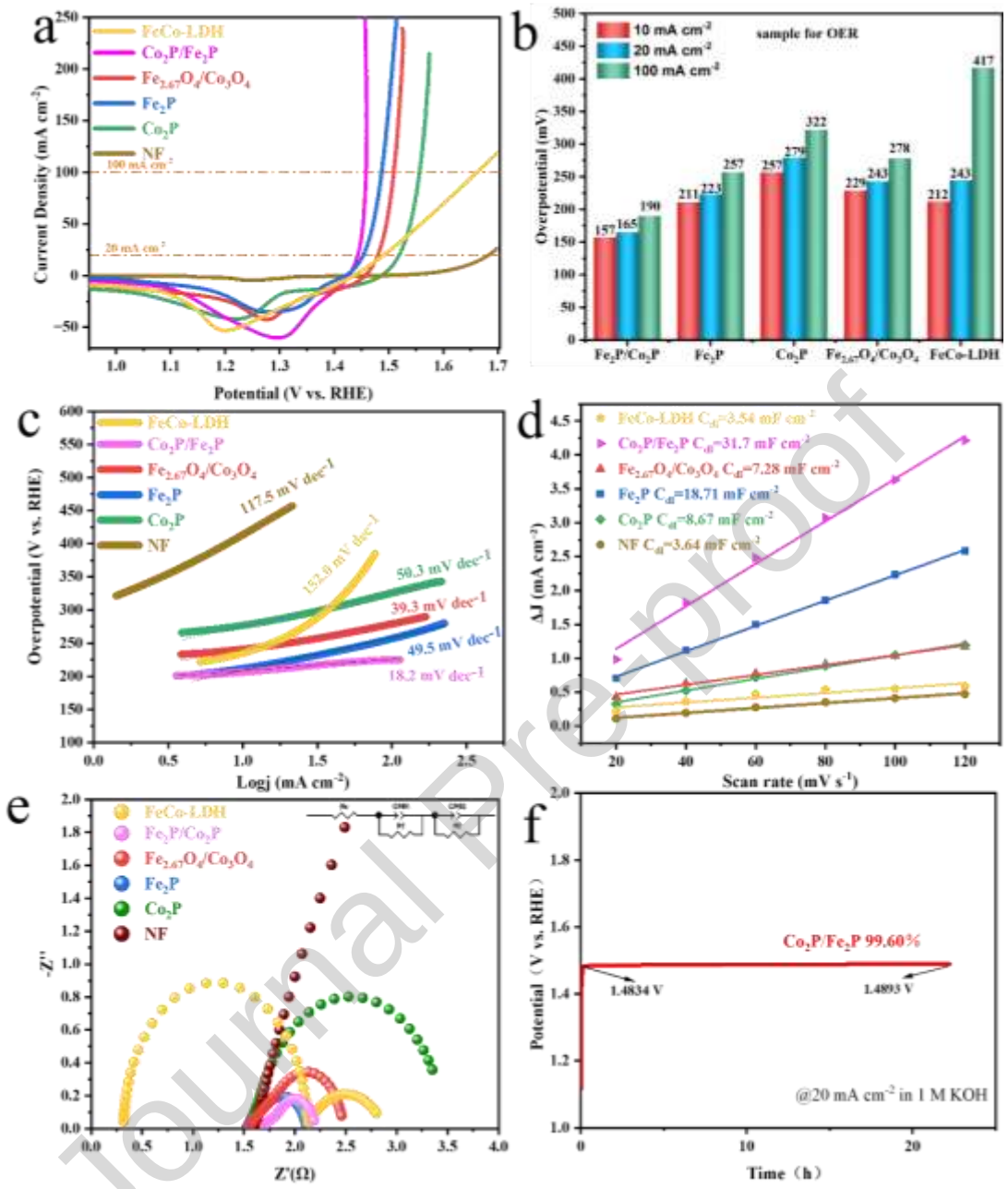

Fig. 5. OER of Co_2P/Fe_2P, Fe_2P, Co_2P, CoFe-LDH, $Fe_{2.67}O_4/Co_3O_4$ and pure NF. (a) LSV curves at a scan rate of 5 mV s^{-1}; (b) the overpotentials at 10, 20, and 80 mA cm^{-2}; (c) Tafel plots; (d) double-layer capacitance measurements (plot of scan rate vs. current density) for OER of Co_2P/Fe_2P, Fe_2P, Co_2P, CoFe-LDH, $Fe_{2.67}O_4/Co_3O_4$ and pure NF; (e) Nyquist plots of Co_2P/Fe_2P, Fe_2P, Co_2P, $Fe_{2.67}O_4/Co_3O_4$, FeCo-LDH, and NF; (f) Chronopotentiometry curve of Co_2P/Fe_2P at 20 mA cm^{-2} for 20 h in 1.0 M KOH.

Finally, a two-electrode electrolyzer applying Co_2P/Fe_2P@NF as both cathode and anode was assembled to investigate the overall water splitting (OWS) performance. As

indicated in Fig. S13a, the LSV curves show that the electrolyzer using Co_2P/Fe_2P/NF as catalysts only requires a cell potential of 1.50 V to drive the current density at 20 mA cm^{-2}, which is significantly lower than the 1.624 V needed for the benchmark Pt/C/NF//RuO_2/NF system. This improvement is attributed to the electronic synergy at heterointerfaces and the efficient transport of the self-supported structure [55, 57-59]. The stability tests of Co_2P/Fe_2P/NF//Co_2P/Fe_2P/NF in Fig. S13b show remarkable long-term durability, with 97.62% potential retention after 20 h of continuous electrolysis, indicating promising potential for practical applications.

3.4. DFT insights into electronic structure and interfacial charge transfer

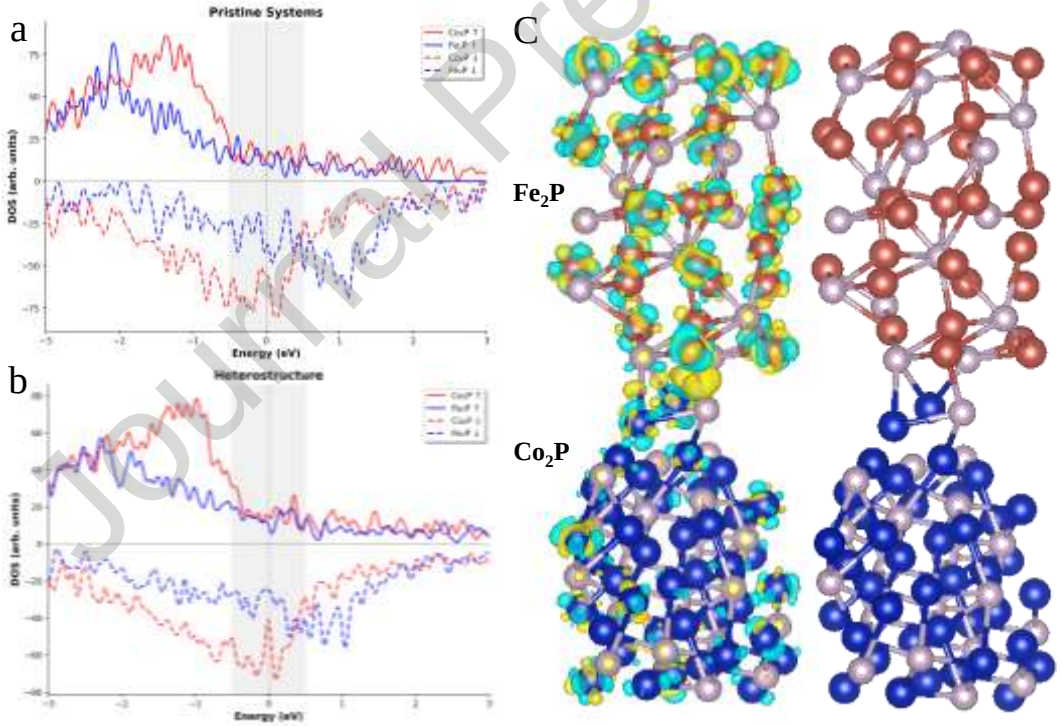

Fig. 6. DFT-calculated Density of States (DOS) and DFT-calculated Charge Density Difference (CDD). (a) Projected DOS for pristine Co_2P and Fe_2P systems. (b) Total DOS for the Co_2P/Fe_2P heterostructure. (c) Side view of the CDD at the Co_2P (112)/Fe_2P (111) interface.

To unravel the origin of the interfacial built-in electric field (BEF) and the

enhanced charge-transport characteristics, we performed spin-polarized DFT calculations on the Co_2P (112) and Fe_2P (111) surfaces and on their coherent interface (computational details in Section 2.6). The electronic structures were analyzed through spin-resolved projected density of states (PDOS) and charge-density-difference (CDD).

The PDOS of the isolated slabs (Fig. 6a) exhibits only a modest density at the Fermi level (E_F) with well-defined band edges. Notably,

E_F is pinned closer to the conduction-band edge in Co_2P, whereas it lies nearer to the valence-band edge in Fe_2P. This alignment is diagnostic of n-type Co_2P and p-type Fe_2P, respectively, and is fully consistent with the Mott-Schottky slopes and the band alignment constructed from UV-Vis analysis (Fig. 3), in line with previous work on work-function-governed interfacial electric fields and internal-field-assisted catalysis [26, 33]. The states around E_F are dominated by transition-metal d orbitals, providing the frontier manifold that participates in interfacial hybridization.

Upon constructing the Co_2P/Fe_2P junction, the total DOS near E_F becomes broadened and enhanced (Fig. 6b), indicating strong interfacial orbital hybridization and the emergence of delocalized states that bridge the band edges of the two constituents. Such hybridized states are expected to lower the electronic transport barrier across the interface and rationalize the experimentally observed reduction of charge-transfer resistance (EIS), which is consistent with the general role of internal electric fields in facilitating interfacial charge transport [60]. Concomitantly, the CDD map (Fig. 6c) reveals electron accumulation on the Fe_2P side and electron depletion on

the Co_2P side, establishing a BEF directed from n-type Co_2P to p-type Fe_2P. The direction of charge transfer ($Co_2P \rightarrow Fe_2P$) agrees with the opposite binding-energy shifts of Co 2p and Fe 2p in XPS, as well as with the KPFM-measured interfacial potential step across the heterojunction.

This interfacial electron redistribution is expected to have important catalytic consequences. The electron accumulation on the Fe_2P side and electron depletion on the Co_2P side indicate distinct local electronic environments across the heterointerface. Together with the increased DOS near E_F supplied by interfacial hybridization, these results are consistent with facilitated interfacial charge transport and intrinsically improved electrocatalytic kinetics in Co_2P/Fe_2P. It should be noted that the present DFT calculations were designed to elucidate the band alignment, interfacial charge redistribution, and electronic coupling associated with the built-in electric field. Therefore, they should be interpreted as qualitative descriptors of the BEF effect rather than direct quantitative proof of the adsorption energetics of specific HER/OER intermediates. Nevertheless, the qualitative trends revealed by PDOS and CDD are well corroborated by the Mott-Schottky, KPFM, XPS, EIS, and ECSA-normalized electrochemical results [60].

4. Conclusions

We demonstrate a binder-free Co_2P/Fe_2P p-n heterojunction on Ni foam that exploits an interfacial built-in electric field (BEF) to accelerate alkaline HER/OER. Mott-Schottky/KPFM identify n-type Co_2P and p-type Fe_2P with a strong interfacial

potential, while DFT (spin-resolved PDOS and CDD) reveals electron transfer from Co_2P to Fe_2P and hybridized states near E_F, which are consistent with improved interfacial charge transport and intrinsically enhanced HER/OER kinetics. Together with the ECSA-normalized electrochemical results, these findings support that the superior catalytic performance of Co_2P/Fe_2P arises not only from its enlarged active surface area, but also from interfacial electronic modulation associated with the built-in electric field. Electrochemically, Co_2P/Fe_2P@NF delivers low overpotentials of η_{20} = 109 mV (HER) and 165 mV (OER), and a two-electrode cell reaches 20 mA cm^{-2} at 1.50 V, retaining ~98% of the initial potential over 20 h.

Despite the encouraging results, the present evidence for the built-in electric field is still mainly based on ex situ or dry-state characterization, and the current DFT calculations focus primarily on band alignment and interfacial charge redistribution rather than explicit adsorption energetics of specific HER/OER intermediates. Future work combining operando interfacial characterization with more quantitative theoretical modeling will be valuable for further clarifying the structure-electronic structure-activity relationship in phosphide heterojunctions.

CRediT authorship contribution statement

Ang Li: Writing - original draft, Data curation, Conceptualization. Hui Min Gu: Supervision, Methodology. Baiyu Ren: Writing - review & editing, Supervision, Methodology. Hao Yu: Methodology. Bao Yue Zhang: Writing - review & editing,

Supervision. Xinyi Hu: Methodology, Formal analysis. Zhong Li: Supervision, Funding acquisition. Yinfen Cheng: Supervision, Formal analysis. Heng Yang: Methodology. Nikhil V. Medhekar: Methodology. Yuefeng Yin: Writing - original draft, Data curation. Jian Zhen Ou: Writing - review & editing, Supervision, Project administration, Funding acquisition.

Declaration of competing interest

The authors declare that they have no known competing financial interests or personal relationships that could have appeared to influence the work reported in this paper.

Acknowledgments

This work is supported by the National Natural Science Foundation of China (52172155, 22462020), Sichuan Science and Technology Program (2025ZNSFSC1390).

Data availability

Data will be made available on request.

References

[1] B. Horri, H. Ozcan, Green hydrogen production by water electrolysis: Current status and challenges, Curr. Opin. Green Sustain. Chem., 47 (2024) 100932.
[2] M. Plevová, J. Hnát, K. Bouzek, Electrocatalysts for the oxygen evolution reaction in alkaline and neutral media. A comparative review, J. Power Sources, 507 (2021) 230072.
[3] Y. Zhu, M. Klingenhof, C. Gao, T. Koketsu, G. Weiser, Y. Pi, S. Liu, L. Sui, J. Hou, J. Li, H. Jiang, L. Xu, W. Huang, C. Pao, M. Yang, Z. Hu, P. Strasser, J. Ma, Facilitating

alkaline hydrogen evolution reaction on the hetero-interfaced Ru/RuO2 through Pt single atoms doping, Nat. Commun., 15 (2024) 1447.
[4] C. Li, J. Baek, Recent Advances in Noble Metal (Pt, Ru, and Ir)-Based Electrocatalysts for Efficient Hydrogen Evolution Reaction, ACS Omega, 5 (2020) 31–40.
[5] H. Li, Z. Qi, P. Pan, H. Li, J. He, R. Zhang, Y. Su, K. Zhu, H. Dong, Z. Yang, Collaborative engineering of Co2P and Co-N-C dual active sites to boost bifunctional activity for air electrodes in rechargeable Zn-air batteries, J. Alloys Compd., 1040 (2025) 183507.
[6] J. Mei, Y. Deng, X. Cheng, X. Wang, Q. Wu, Recent advances in iron-based sulfides electrocatalysts for oxygen and hydrogen evolution reaction, Chin. Chem. Lett., 35 (2024) 108900.
[7] Q. Li, Y. Chen, Y. Zhu, S. Yuan, X. Song, H. Wang, T. Tang, Research progress and application of non-noble transition metal-based electrocatalysts in the hydrogen evolution reaction by water splitting, Sustainable Energy Fuels, 10 (2026) 1635–1675.
[8] H. Han, J. Choi, M. Son, K. Kim, Unlocking power of neighboring vacancies in boosting hydrogen evolution reactions on two-dimensional NiPS 3 monolayer, eScience, 4 (2024) 100204.
[9] B. Liu, X. Lan, Q. Zhong, T. Wang, Metal Phosphide: An Atypical Catalytic Site, ACS Catal., 14 (2024) 757–775.
[10] C. Bai, Y. Wu, Y. Xin, J. Mou, L. Xia, D. Ding, X. Zheng, P. Yu, Alkali metal doped copper-sulfides as a new class electrocatalysts for oxygen evolution reaction, J. Alloys Compd., 962 (2023) 171171.
[11] Z. Wan, X. Guo, J. Jiang, Y. Xin, B. Tang, H. Zhang, Y. Wu, L. Xia, P. Yu, Modulating nickel-iron active species via dealloying to boost the oxygen evolution reaction, Dalton Trans., 53 (2024) 2065–2072.
[12] Y. Wu, Q. Chen, Q. Zhang, C. Bai, J. Peng, B. Tanga, D. Li, D. Ding, L. Xia, X. Guo, P. Yu, Self-supported electrode Fe35Co20Ni20Mo20Si5 alloy ribbon: Electronic structure modulating oxygen evolution reaction, J. Alloys Compd., 911 (2022) 164993.
[13] C. Bai, Y. Wu, Dealloying strategy triggers active site switching to boost oxygen evolution reaction, J. Alloys Compd., 1037 (2025) 182255.
[14] W. Zhang, Y. Chen, Z. Ma, Z. Sun, J. Wang, J. Feng, W. Yan, H. Wang, Challenges and strategies of transition metal phosphides applied in oxygen evolution reaction of electrocatalytic water splitting: A review, Fuel, 369 (2024) 131741.
[15] T. Aziz, M. Haque, S. Saha, B. Mondal, S. Jain, A. Dutta, A Review of Nanostructured Transition Metal Phosphide-Driven Electrocatalytic Oxygen Evolution Reaction, Energy Fuels, 37 (2023) 18291–18309.
[16] A. Dong, T. Yang, J. Xue, H. Gao, L. Che, Transition metal phosphide electrocatalysts for efficient oxygen evolution reaction, Appl. Surf. Sci., 708 (2025) 163769.
[17] B. An, X. Li, L. Li, Z. Dai, N. Li, Y. Gao, L. Ge, Review and perspective on the

rational design and structural modulation of transition metal phosphides for efficient electrocatalytic water splitting, Coord. Chem. Rev., 550 (2026) 217406.
[18] X. Wang, Z. Zhang, H. Zhang, S. Lin, C. Li, Y. Xie, Y. Zhang, S. Feng, D. Liu, Z. Wang, Crystalline/Amorphous Phosphide Heterostructures with Built-in Electric Fields for Efficient and Long-Term Industrial-Scale Alkaline Water Electrolysis, Adv. Funct. Mater., 36 (2025) 2514137.
[19] Y. Xu, Y. Zhao, S. Peng, M. Sun, G. Cheng, Y. Zhong, L. Yu, Constructing a NiCoP/FeP p-n heterojunction with built-in electric field regulation as an efficient alkaline hydrogen evolution electrode, J. Mater. Chem. A, 13 (2025) 18714–18721.
[20] L. Wang, C. Liu, J. Sun, Y. Ji, N. Zhao, J. Xin, Y. Jiao, C. Lv, X. Wang, Accelerating electron transfer for high-efficiency overall water splitting via built-in electric field in Ni2P/CoP2 heterojunction nanoarray, Int. J. Hydrogen Energy, 229 (2026) 154729.
[21] Y. Sun, F. Yang, K. Wei, S. Sun, L. Sun, J. An, C. Yu, Q. Guo, C. Zhang, G. Ma, H. Liu, Y. Li, Construction of a built-in electric field in Mo-doped Ni/WO3 to enhance asymmetric charge distribution for efficient overall water splitting, Chem. Sci., 17 (2026) 2210–2221.
[22] C. Ni, K. Wang, L. Jin, Y. Liu, J. Chen, L. Yang, C. Ji, H. Xu, Z. Li, L. Tian, Built-in electric field guides oxygen evolution electrocatalyst reconstruction, Chem. Commun., 61 (2025) 658–668.
[23] Y. Zhang, Y. Qi, H. Zhou, Y. Zhang, J. Sun, W. Ma, J. Hu, L. Feng, F. Yu, Built-in electric field engineering in Co2N0.67/CoP heterostructures for glycerol electrooxidation-assisted hydrogen production, Nat. Commun., (2026).
[24] S. Hou, A. Zhang, Q. Zhou, Y. Wen, S. Zhang, L. Su, X. Huang, T. Wang, K. Rui, C. Wang, H. Liu, Z. Lu, P. He, Designing heterostructured FeP-CoP for oxygen evolution reaction: Interface engineering to enhance electrocatalytic performance, Nano Res., 16 (2023) 6601–6607.
[25] L. Wang, W. He, D. Yin, Q. Ma, W. Yu, Y. Yang, X. Dong, Synergistic Effect between Co2P/Fe2P Nanoparticles and NiFe Layered Double Hydroxides Promotes Urea Oxidation Reaction-Assisted Hydrogen Production, ACS Appl. Nano Mater., 8 (2025) 2861–2872.
[26] Z. Chen, T. Ma, W. Wei, W. Wong, C. Zhao, B. Ni, Work Function-Guided Electrocatalyst Design, Adv. Mater., 36 (2024) 2401568.
[27] R. Yu, X. Cao, C. Zhu, Q. Chen, Z. Yan, B. Jiang, J. Mao, X. Wei, Asymmetric interfacial engineering regulated charge distribution on Ru/Ni-N-C sites for efficient hydrogen evolution reaction in alkaline and seawater electrolytes, Sci. China Chem., 68 (2025) 3048–3055.
[28] Y. Li, Y. Wang, X. Li, Y. Zhang, P. Li, Improve the catalytic performance of Co-Co2P based catalysts via introduction of Ca element toward advanced oxidation of tetracycline, J. Alloys Compd., 1039 (2025) 183059.
[29] W. Abdullah, A. Aghamiri, L. Putri, A. Mohamed, A. Shafawi, Exploring transition metal phosphides: A non-noble metal approach to high-performance bifunctional

alkaline water splitting, Int. J. Hydrogen Energy, 215 (2026) 153894.
[30] Y. Liu, Y. Hu, X. Zhao, S. Zhu, Y. Min, Q. Xu, Q. Li, Oxygen Vacancy and Heterostructure Modulation of Co2P/Fe2P Electrocatalysts for Improving Total Water Splitting, ACS Appl. Mater. Interfaces, 16 (2024) 13795–13805.
[31] H. Yang, P. Guo, R. Wang, Z. Chen, H. Xu, H. Pan, D. Sun, F. Fang, R. Wu, Sequential Phase Conversion-Induced Phosphides Heteronanorod Arrays for Superior Hydrogen Evolution Performance to Pt in Wide pH Media, Adv. Mater., 34 (2022) 2107548.
[32] B. Hao, M. Gan, J. Guo, G. Li, Y. Song, Y. Shen, B. Xu, P. Liu, J. Guo, Constructing 2D PtSe2/PtCo Heterojunctions by Partial Selenization for Enhanced Hydrogen Evolution, Adv. Funct. Mater., 35 (2025) 2413916.
[33] D. Chen, R. Lu, R. Yu, Y. Dai, H. Zhao, D. Wu, P. Wang, J. Zhu, Z. Pu, L. Chen, J. Yu, S. Mu, Work-function-induced Interfacial Built-in Electric Fields in Os-OsSe2 Heterostructures for Active Acidic and Alkaline Hydrogen Evolution, Angew. Chem. Int. Ed., 61 (2022) e202208642.
[34] H. Li, H. Li, M. Du, E. Zhou, W. Leow, M. Liu, A perspective on field-effect in energy and environmental catalysis, Chem. Sci., 16 (2025) 1506–1527.
[35] X. Zhao, M. Liu, Y. Wang, Y. Xiong, P. Yang, J. Qin, X. Xiong, Y. Lei, Designing a Built-In Electric Field for Efficient Energy Electrocatalysis, ACS Nano, 16 (2022) 19959–19979.
[36] W. Liu, J. Dong, B. An, H. Su, Z. Teng, N. Li, Y. Gao, L. Ge, Synergistic dual built-in electric fields in 1T-MoS2/Ni3S2/LDH for efficient electrocatalytic overall water splitting reactions, J. Colloid Interface Sci., 673 (2024) 228–238.
[37] Y. Pan, K. Sun, S. Liu, X. Cao, K. Wu, W. Cheong, Z. Chen, Y. Wang, Y. Li, Y. Liu, D. Wang, Q. Peng, C. Chen, Y. Li, Core-Shell ZIF-8@ZIF-67-Derived CoP Nanoparticle-Embedded N-Doped Carbon Nanotube Hollow Polyhedron for Efficient Overall Water Splitting, J. Am. Chem. Soc., 140 (2018) 2610–2618.
[38] L. Luo, X. Cheng, Q. Wu, Ru-modified NiO electrocatalysts for HER: Lower energy barriers and prolonged stability, Chin. Chem. Lett., 37 (2026) 111308.
[39] Y. Shi, B. Zhang, Recent advances in transition metal phosphide nanomaterials: synthesis and applications in hydrogen evolution reaction, Chem. Soc. Rev., 45 (2016) 1529–1541.
[40] Z. Chen, R. Wu, Y. Liu, Y. Ha, Y. Guo, D. Sun, M. Liu, F. Fang, Ultrafine Co Nanoparticles Encapsulated in Carbon-Nanotubes-Grafted Graphene Sheets as Advanced Electrocatalysts for the Hydrogen Evolution Reaction, Adv. Mater., 30 (2018) 1802011.
[41] B. Zhang, J. Wang, G. Liu, C. Weiss, D. Liu, Y. Chen, L. Xia, P. Zhou, M. Gao, Y. Liu, J. Chen, Y. Yan, M. Shao, H. Pan, W. Sun, A strongly coupled Ru-CrOx cluster-cluster heterostructure for efficient alkaline hydrogen electrocatalysis, Nat. Catal., 7 (2024) 441–451.
[42] J. Li, C. Gao, H. Wang, B. Li, S. Zhao, Y. Kim, Z. Liu, X. Du, Z. Peng, Surface

Modulation of 3D Porous CoNiP Nanoarrays In Situ Grown on Nickel Foams for Robust Overall Water Splitting, Int. J. Mol. Sci., 23 (2022) 5290.
[43] Z. Liu, Y. Dai, X. Han, C. Hou, K. Li, Y. Li, H. Wang, Q. Zhang, CoFe hydroxide towards CoP2-FeP4 heterojunction for efficient and long-term stable water oxidation, J. Colloid Interface Sci., 676 (2024) 937–946.
[44] S. Fu, C. Peng, Y. Luo, L. Cheng, X. Yang, Z. Jiao, Regular Modulating space charge of FeP/CoP p-n heterojunction for boosting oxygen evolution reaction, J. Colloid Interface Sci., 664 (2024) 349–359.
[45] W. Yu, Q. Li, W. Xiao, J. Wang, B. Dong, Y. Chai, Z. Wu, L. Wang, Unique CoP Microflower Decorated with Phosphorous-Enriched PtP2 onto Nickel Foam with Interfacial Electronic Interactions to Boost Alkaline Water-Splitting, Adv. Funct. Mater., 34 (2024) 2313935.
[46] L. Yan, L. Cao, P. Dai, X. Gu, D. Liu, L. Li, Y. Wang, X. Zhao, Metal-Organic Frameworks Derived Nanotube of Nickel-Cobalt Bimetal Phosphides as Highly Efficient Electrocatalysts for Overall Water Splitting, Adv. Funct. Mater., 27 (2017) 1703455.
[47] Z. Ding, H. Yu, X. Liu, N. He, X. Chen, H. Li, M. Wang, Y. Yamauchi, X. Xu, M. Amin, T. Lu, L. Pan, Prussian blue analogue derived cobalt-nickel phosphide/carbon nanotube composite as electrocatalyst for efficient and stable hydrogen evolution reaction in wide-pH environment, J. Colloid Interface Sci., 616 (2022) 210–220.
[48] G. Lee, S. Jun, Y. Kim, I. Park, H. Jang, S. Park, K. Kwon, Multicomponent Metal Oxide- and Metal Hydroxide-Based Electrocatalysts for Alkaline Water Splitting, Materials, 16 (2023) 3280.
[49] W. Zou, C. Sun, K. Zhao, J. Li, X. Pan, D. Ye, Y. Xie, W. Xu, H. Zhao, L. Zhang, J. Zhang, Surface reconstruction of NiCoP pre-catalysts for bifunctional water splitting in alkaline electrolyte, Electrochim. Acta, 345 (2020) 136114.
[50] J. Mei, X. Cheng, Q. Wu, Dual-doped spinel nickel-iron oxide nanoflowers for remarkably enhanced oxygen evolution reaction, J. Alloys Compd., 1010 (2025) 177292.
[51] J. Mei, X. Cheng, Q. Wu, Vanadium-doped FeO/NiS nanosheet arrays: Synergistic heterometal doping and heterostructure design for enhanced oxygen evolution catalysis, J. Alloys Compd., 1008 (2024) 176386.
[52] M. Wu, G. Zhang, N. Chen, Y. Hu, T. Regier, D. Rawach, S. Sun, Self-Reconstruction of Co/Co2P Heterojunctions Confined in N-Doped Carbon Nanotubes for Zinc-Air Flow Batteries, ACS Energy Lett., 6 (2021) 1153–1161.
[53] Z. Pu, C. Zhang, I. Amiinu, W. Li, L. Wu, S. Mu, General Strategy for the Synthesis of Transition-Metal Phosphide/N-Doped Carbon Frameworks for Hydrogen and Oxygen Evolution, ACS Appl. Mater. Interfaces, 9 (2017) 16187–16193.
[54] S. Yang, J. Luo, Y. Xu, M. Wu, Y. Yang, Oxygen evolution reaction performance misjudgment caused by the self-oxidation process, Nano Res. Energy, 3 (2024) e9120136.

[55] Y. Wu, X. Guo, H. Chen, Y. Xin, X. Dong, X. Hu, L. Xia, P. Yu, Molybdenum triggers the bifunctional mechanism of oxygen evolution reaction of Fe 34-x Ni 25 Co 25 Mo x B 8 P 8 amorphous alloy with boosted catalytic activity, J. Electroanal. Chem., 972 (2024) 118612.
[56] M. Wu, Y. Xu, J. Luo, S. Yang, G. Zhang, L. Du, H. Luo, X. Cui, Y. Yang, S. Sun, A Rechargeable Urea-Assisted Zn-Air Battery With High Energy Efficiency and Fast-Charging Enabled by Engineering High-Energy Interfacial Structures, Angew. Chem. Int. Ed., 63 (2024) e202410845.
[57] W. Hu, Q. Jiang, L. Wang, S. Hu, Z. Huang, T. Zhou, H. Yang, J. Hu, N. Tang, Hierarchical Ni-Co-O-C-P hollow tetragonal microtubes grown on Ni foam for efficient overall water splitting in alkaline media, RSC Adv., 9 (2019) 26051–26060.
[58] H. Zhang, N. Li, S. Gao, A. Chen, Q. Qian, Q. Kong, B. Xia, G. Hu, Quenching-induced atom-stepped bimetallic sulfide heterointerface catalysts for industrial hydrogen generation, eScience, 5 (2025) 100311.
[59] W. Li, Y. Deng, L. Luo, Y. Du, X. Cheng, Q. Wu, Nitrogen-doped Fe2O3/NiTe2 as an excellent bifunctional electrocatalyst for overall water splitting, J. Colloid Interface Sci., 639 (2023) 416–423.
[60] L. Chen, J. Ren, Z. Yuan, Enabling Internal Electric Fields to Enhance Energy and Environmental Catalysis, Adv. Energy Mater., 13 (2023) 2203720.

Declaration of Interest Statement

☑ The authors declare that they have no known competing financial interests or personal relationships that could have appeared to influence the work reported in this paper.

Highlights

- Co_2P/Fe_2P p-n heterojunction arrays are built on Ni foam via phosphorization.

- Interfacial built-in electric field is quantitatively confirmed by KPFM.
- BEF optimizes charge distribution to boost bifunctional catalytic activities.
- The electrolyzer achieves 20 mA cm^{-2} at a low cell voltage of 1.50 V.